ELSEVIER

Contents lists available at ScienceDirect

International Journal of Heat and Mass Transfer

journal homepage: www.elsevier.com/locate/hmt



Thermal atomization during droplet impingement on superhydrophobic surfaces: Influence of Weber number and micropost array configuration



Preston Emerson*, Julie Crockett, Daniel Maynes

Brigham Young University, Department of Mechanical Engineering Engineering Building, Campus Dr, Provo, UT 84602, United States

ARTICLE INFO

Article history:
Received 29 June 2020
Revised 16 September 2020
Accepted 29 September 2020
Available online 28 October 2020

Keywords: Atomization Droplets Superhydrophobic Thermal Impingement Boiling

ABSTRACT

An experimental study of thermal atomization intensity during droplet impingement on superheated hydrophobic and superhydrophobic surfaces of varying microstructure was performed. Thermal atomization in these scenarios is the result of droplet boiling, where vapor bubbles burst upwards through the droplet lamella, causing a fine spray of secondary droplets. A smooth hydrophobic surface and three post-patterned superhydrophobic surfaces of similar solid fraction but differing post size were investigated over a range of surface temperatures from 120 °C to 320 °C and Weber numbers from 20 to 200. Trends in atomization intensity were characterized using a high-speed image processing technique. Changes in surface temperature, Weber number, and microstructure configuration were shown to significantly influence atomization intensity, and these parameters are thought to be directly linked to three main mechanisms accounting for atomization dynamics in impingement scenarios. These mechanisms are vapor generation at the liquid-solid interface of the impinging droplet, vapor bursting through the spreading lamella, and vapor escape laterally beneath the droplet. Vapor generation increases with an increase in heat transfer to the droplet, which may be produced by increasing surface temperature or increasing liquid-solid contact through droplet wetting. Vapor bursting upwards through the lamella depends mainly on lamella thickness which decreases with increasing Weber number. Finally, vapor escape beneath the droplet may occur as vapor flows laterally through the micropost arrays. This is found to be enhanced by increasing the spacing between structures. These competing mechanisms result in thermal atomization, which generally increases with increasing Weber number and decreasing pitch. Additionally, the Leidenfrost point was also found to increase with increasing Weber number and decreasing pitch. A scale analysis was performed to explore the effect of resistance to vapor escape through micropost arrays on thermal atomization, and the resulting scaling describes the experimental findings well.

© 2020 Elsevier Ltd. All rights reserved.

1. Introduction

When a water droplet impacts a solid surface it may stick, bounce, or splash depending on the surface energy and roughness as well as droplet properties and impact velocity [1,2]. Specifically, surface roughness can alter the spreading and receding droplet shape, rate, and bouncing dynamics [1,3–5]. A heated surface results in slightly different dynamics. At surface temperatures below the saturation temperature liquid properties may vary, changing the dynamics accordingly. At surface temperatures above the saturation temperature, boiling can occur, significantly altering the classical droplet spreading and splashing or bouncing processes.

E-mail address: ptemerson217@byu.edu (P. Emerson).

Below, we introduce the pertinent effects of surface structure on heat transfer to liquids.

For sessile droplets undergoing subcritical heating on a structured surface, the local wetting state is important. Heat transfer increases as liquid-solid contact increases, corresponding to increased wetting (or Wenzel state) [6–9], which is a function of the structure type and liquid properties [10]. By altering the microstructure shape and design, the wetting state can be changed, thus altering the total heat transfer [11–13]. When droplets impinge on a micro or nanostructured superhydrophobic (SH) surface where the Cassie-Baxter, or non-wetting, state generally prevails, the increased pressure at the point of impingement may cause local wetting resulting in higher heat transfer, where a decrease in microstructure area fraction increases this likelihood [14–16]. Fig. 1 shows the three SH microstructure configurations used in this study along with important microstructure parameters: struc-

^{*} Corresponding author.

Fig. 1. SEM images of micropost arrays for (a) 8 µm (b) 12 µm and (c) 16 µm pitch surfaces. The scale bar on (a) applies to all three images.

ture shape (circular posts), height (h), pitch, or center-to-center spacing (w), and diameter (d). Solid fraction, or the ratio of liquid-solid contact area to total projected surface area (f_s) is often used to define SH structures as well.

During supercritical heating, it has been shown that for SH surfaces, surface microstructure configuration significantly affects the classic boiling regimes (convective, nucleate, transition, and film) for pool boiling [15,17,18], sessile drops [6,7,15], and impinging drops on smooth [19-23] and rough surface [24-26] scenarios. Here we focus on droplets and two particular regimes of interest: nucleate boiling and the onset of film boiling, or the Leidenfrost point (LFP). In the nucleate boiling regime, rising vapor bubbles may burst through the lamella of the impinging droplet causing a fine spray of water droplets called thermal atomization, which can be quantified, and provides insight into the strength of nucleate boiling [19,22,26,27], where heat transfer is greatest. The LFP represents a heat transfer minimum and can be defined as the total suppression of thermal atomization in droplet impingement situations. Heat transfer during droplet impingement plays an important role in many applications including spray cooling of metals and fuel injection in combustion engines [28,29].

For droplet impingement on a smooth wall heated above the saturation temperature, high pressure in the surrounding air results in a lower temperature onset of LFP [28,29] while at low pressure explosive drop bouncing occurs due to a large vapor bubble encapsulated beneath the drop (instead of complete film as in LFP scenarios) which erupts when the drop impinges [30]. Although the wall temperature has an effect on boiling, droplet detachment is defined primarily by the Weber number, defined as $We = \rho V_0^2 D_0/\sigma$ where ρ and σ are the droplet density and surface tension, respectively, D_0 is initial droplet diameter, and V_0 is droplet impact velocity [31].

During sessile droplet heating on a SH surface, nucleate boiling is suppressed, and even completely mitigated for surfaces with extremely low solid fraction, and LFP occurs at a significantly lower temperature [6,32–35]. Similar dynamics occur for impinging droplet scenarios on SH surfaces. In a 2018 study by Clavijo et al. [26], thermal atomization during droplet impingement was quantified for a smooth hydrophobic (SmH) and three post-patterned SH surfaces of similar solid fraction and varying pitch. The impact Weber number was held constant for all experiments. It was shown that for the SH surfaces, atomization intensity in an impingement scenario decreases with increasing microstructure pitch. This behavior was attributed to the increased ability for vapor escape beneath the droplet between the micropost structures. An analytical model by Ishino et al. [36] for viscous fluid flow through a micropost array was used to justify this finding, demonstrating the inverse relationship between microstructure pitch and resistive viscous force due to the microstructures. Clavijo also showed that the LFP decreases with increasing pitch.

As previously noted, the wetting state of a structured surface can significantly alter heat transfer dynamics since wetting often occurs at the stagnation point of an impinging droplet [3,37-39]. Localized wetting leads to temporarily higher liquid-solid contact area in the stagnation region, enhancing heat transfer and increasing thermal atomization intensity. Subsequently, dewetting can occur as liquid exits the cavities and if this happens the Cassie-Baxter state returns. In a 2009 study, Deng et al. [37] asserted that, initially, wetting in the stagnation region is driven mainly by the water hammer pressure, resulting from liquid compression behind the shock envelope that develops upon impact [40]. Within approximately 1 ms, the water hammer pressure dissipates, and the local dynamic pressure governs wetting behavior in the droplet spreading phase. It was also shown that with increasing impact velocity, the degree of drop penetration into the microstructures increases. When this happens full wetting below the impingement region prevails, although this region may still dewet, and complete droplet bouncing is still possible [3]. Pittoni et al. [38] found that for SH graphite surfaces at room temperature, the rate of dewetting for impinging droplets increases with increasing Weber number. Clavijo et al. [39] showed that for post-patterned SH surfaces at subcritical temperatures, dewetting rate increases with surface temperature. Clavijo also showed that the roughness factor of the surface, $r = 1 + \pi dh/w^2$, is an important parameter in determining dewetting rates. Clavijo's model showed that increasing the roughness factor increases the surface energy gradient between the Wenzel and Cassie states, which in turn increases the rate of dewetting

(c)

In this paper, we discuss thermal atomization during droplet impingement on SH surfaces in the context of three important mechanisms: vapor generation due to boiling at the liquid-solid interface of the spreading droplet, vapor bursting upwards through the lamella, and vapor escape laterally beneath the droplet. Fig. 2 illustrates these mechanisms for a droplet impinging a SH surface in the nucleate boiling regime. Regarding the first mechanism, it was previously stated that enhanced liquid-solid contact area. specifically due to wetting at the impingement point in superhydrophobic scenarios, can act to increase vapor generation through enhanced heat transfer. This enhanced contact is a function of microstructure shape and size, as well as We. The second mechanism is directly related to lamella thickness. As the droplet spreads, the lamella grows thin [1], and vapor bubbles forming in the lamella rise and burst, causing thermal atomization. Lamella thickness is a function of Weber number, where increasing Weber number yields a thinner lamella, and thus less resistance to bursting vapor bubbles and greater thermal atomization intensity [41].

Vapor escape beneath the droplet is depicted in the schematic on the right of Fig. 2. Vapor generated in the spreading droplet may flow laterally through the cavities between microstructures (see Fig. 1). Resistance to vapor flow is increased by narrowing structure pitch and may be completely blocked by localized wetting. Surface microstructure configurations that allow greater vapor escape are hypothesized to suppress thermal atomization during droplet impingement by decreasing the volume of vapor that

Fig. 2. Schematic of a droplet impinging a microstructured SH surface in the nucleate boiling regime, such as the ones shown in Fig. 1. White circles represent vapor bubbles generated at the surface due to boiling.

Table 1Micropost array dimensions measured with an optical profilometer for each SH surface.

Surface	Pitch (µm)	Diameter (μ m)	Solid Fraction
8 µm pitch	8.0	3.3	0.13
12 μm pitch	11.9	4.1	0.09
16 µm pitch	15.9	3.4	0.04

is forced through the lamella. However, as microstructure pitch increases, both droplet wetting and vapor escape occur more easily, resulting in competing effects on the generation of thermal atomization such that the dominant effect is often not readily apparent.

In this paper, thermal atomization during droplet impingement on a SmH and three post-patterned SH surfaces is explored for a range of Weber numbers from 20 to 200 and surface temperatures between 120 °C and 320 °C. While previous work has been mainly concerned with whether or not atomization exists in a given scenario, here it is shown that using an image processing technique, the relative intensity of atomization can be determined. We further show that by adjusting surface temperature, Weber number, and microstructure configuration, atomization intensity can be dramatically altered while maintaining a constant static contact angle. The atomization intensity is discussed in the context of three driving mechanisms: noted above. A scaling analysis is presented that considers resistance to vapor flow through the micropost arrays and this analysis yields good agreement with experimental observations. The paper will proceed as follows: Section 2 describes the methodology employed, including the experimental setup and image processing technique, Section 3 presents experimental results and discussion, Section 4 outlines the derivation and results of the scaling analysis, and conclusions are given in Section 5.

2. Methodology

This section outlines the fabrication process for SH surfaces, the droplet impact experimental setup, and the image processing technique used to evaluate thermal atomization intensity.

2.1. Substrate fabrication

Surface superhydrophobicity can be produced by applying micro- or nano-roughness and a thin hydrophobic coating. This promotes the presence of the Cassie-Baxter state, yielding a reduced liquid-solid contact area. Scanning electron microscope (SEM) images of the surface microstructures created here are shown in Fig. 1. Photolithography is used to deposit a micropost array mask onto a silicon wafer, which is then etched via deep reactive ion etching to $h\approx 4$ µm. A layer of chromium (nominal thickness of 100 nm) is then deposited on the surface, which promotes adhesion of Teflon. The Teflon is applied via a spin coating process, resulting in a thickness of nominally 200 nm.

Table 1 provides micropost array dimensions (measured using an optical profilometer with uncertainty of \pm 1%) for each SH surface considered. Sessile contact angles of the SH surfaces are 150° \pm 3°, with advancing/receding angle hysteresis between 6°

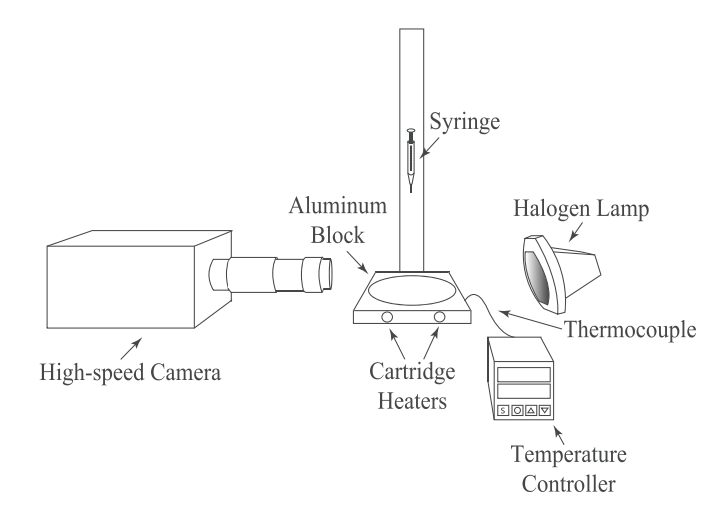


Fig. 3. Schematic of the experimental setup consisting of a high-speed camera, needle to dispense water droplets, heating block with embedded cartridge heaters and thermocouple, halogen backlight, and a temperature controller.

and 15°. A SmH surface with a sessile contact angle of 115° \pm 3° was also fabricated by coating a smooth silicon wafer with Teflon.

2.2. Experimental apparatus

A schematic of the experimental setup is shown in Fig. 3. Water droplets of nearly constant diameter, $D_0 = 2.3 \pm .02$ mm, are dispensed from a syringe whose height can be adjusted to vary the impact Weber number. The silicon substrate sits atop an aluminum heating block, heated with cartridge heaters and kept at constant temperature using a SOLO 9696 temperature controller. A K-type thermocouple is embedded in the aluminum block. Impingement events are captured at 3000 fps using a Photron APX RS high-speed camera. A halogen lamp is positioned behind the droplet, and light is diffused through sand-blasted glass, producing uniform background lighting. Spatial resolution for all scenarios is nominally 12 µm/pixel. Weber numbers of 20, 40, 85, 150, and 200 are considered for each surface with uncertainty ranging from \pm 1.9 (We=20) to \pm 6.1 (We=200). The Ohnesorge $(Oh = We^{1/2}/Re = \mu/(\rho\sigma D)^{1/2})$ and Bond $(Bo = \rho gD^2/\sigma)$ numbers are constant at 0.0024 and 0.71 respectively, showing the significant dominant effect of surface tension relative to viscous and gravitational effects. Impingement events are captured for surface superheat temperatures from 120 $^{\circ}\text{C}$ to 320 $^{\circ}\text{C}$ \pm 3% in increments of 20 °C. The temperature range is restricted by the Teflon, which degrades at temperatures above nominally 340 °C. Between 10 and 20 trials are captured at each temperature and the results are averaged.

2.3. Image processing

High-speed images were analyzed for thermal atomization intensity using MATLAB, similar to the method used by Clavijo et al.

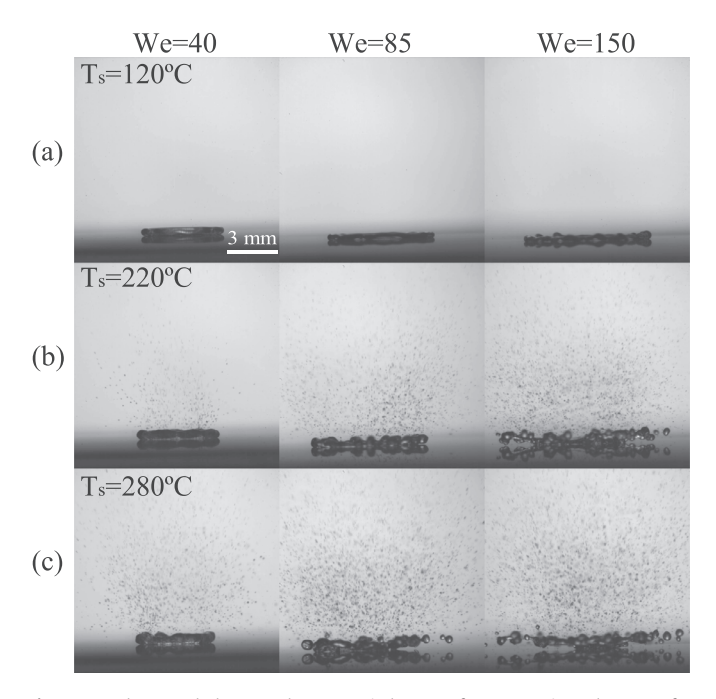


Fig. 4. Droplet morphology on the 8 μ m pitch SH surface approximately 3 ms after impact at surface temperatures of (a) 120 °C (b) 220 °C and (c) 280 °C, and for We=40, 85, and 150. Atomization can be seen clearly above the spreading droplet in (b) and (c).

[26]. A summary of the analysis method is included here. Impingement events are saved in grayscale TIFF format, beginning with the frame just before the droplet enters the field of view (the background image) to a sufficient time after impact to allow for all atomization behavior to be observed. Fig. 4 shows high-speed images of different impingement events on the 8 µm pitch surface at maximum droplet spread for a range of surface temperatures and Weber numbers. Here, the difference between the primary (spreading) droplet and the atomized particles can be easily distinguished, where atomized particles are seen in a fine spray above the primary droplet. At high Weber numbers and temperatures, droplet breakup can occur, characterized by secondary droplets ejecting laterally from the periphery of the primary, likely due to the Rayleigh-Plateau-Savart instability which is characterized by the dominance of surface tension [42-44]. These droplets are generally much larger than those of thermally induced atomization, and are readily apparent at the periphery of the main droplet in Fig. 4b and c at the higher Weber numbers and thus are easily separated from the thermal atomization which is the focus here. Thermal atomization intensity, A, represents the amount of atomization present in a given frame. Note that the image processing technique described below is two-dimensional and sensitive to environmental variables in the experimentation stage, the most important of which are background lighting and spatial resolution.

Each frame is cropped to a field of view of about 10.2×10.2 mm with the droplet centered horizontally. The background image is subtracted from each subsequent image to reduce noise. The total intensity of in-plane atomization in the frame, A, is then found by summing the values of pixels in the background-subtracted frame that contain atomization. Because of the three-dimensional nature of the atomization spray, some atomized particles appear more in-focus (and thus darker) in the two-dimensional high-speed images. Pixels associated with these particles hold a higher value in the background-subtracted frame, so they are weighted more heavily in the final value of A.

Thermal atomization results will be presented in this study with a normalized value $A^*=A/A_{\rm max}$, where $A_{\rm max}$ is the maximum atomization of the maximum atomization atomization of the maximum atomization of the maximum atomization atomization of the maximum atomization of the maximum atomization atomization atomization atomization of the maximum atomization atom

mum value of A over the range of surface temperatures considered for the SmH surface at We=85. This is the same scenario Clavijo [26] used to normalize, and it represents a transition Weber number where droplet breakup begins. When droplet breakup occurs, the primary droplet is often seen beginning to levitate above the surface rather than rebounding. As can be seen from Fig. 4, where We<85, breakup behavior was rarely observed, and the droplet retracts and rebounds off the surface. For We>85, breakup occurs at most surface temperatures explored. It is observed that for Weber numbers where droplet breakup occurs, the likelihood of breakup increases with surface temperature. For We=85, breakup occurs only at the highest surface temperatures explored.

3. Results and discussion

Atomization intensity for a given scenario is dependent on the amount of vapor generated, the amount of vapor that breaks through the lamella, and the ability for vapor to escape beneath the droplet. In this section, experimental results will be presented and discussed in the context of these three important mechanisms.

First, we consider the temporal progression of an impinging droplet in the nucleate boiling regime, as shown in Fig. 5, for the SmH and 8 μ m pitch SH surfaces for $T_s = 240$ °C and We = 85, where both surfaces exhibit similar atomization intensity. Atomization is already being generated at t = 2 ms as the droplet spreads and vapor bubbles travel upward through the lamella and burst at the free surface. By t = 4 ms, atomized particles are leaving the field of view. The rate at which atomized particles leave the field of view is indicative of the velocity with which the particles are traveling. At t = 6 ms the primary droplet has begun to levitate.

Fig. 6 displays A^* throughout the life of the droplet at the temperature for which maximum atomization was observed on each surface ($T_{\rm S}=220~^{\circ}{\rm C}$ for the SmH, $T_{\rm S}=280~^{\circ}{\rm C}$ for the 8 µm pitch, and $T_{\rm S}=180~^{\circ}{\rm C}$ for the 12 µm and 16 µm pitch surfaces). Time, t, is measured from droplet impact, with a timestep of $\Delta t=0.33$ ms. Plot insets show results for low-atomizing cases (12 µm and 16 µm pitch surfaces). Note that $A^*<0.001$ is assumed to be zero. The results presented in Fig. 6 demonstrate that A^* initially increases with time, as atomization is generated, and reaches a maximum value, A^{*} max.t, before decreasing, due to atomized particles leaving the field of view.

The maximum atomization intensity is significantly affected by both surface microstructure and Weber number, as illustrated in Fig. 6. For all surfaces considered, atomization intensity increases with increasing Weber number, especially in the lower range of Weber numbers explored here. This is attributed to the fact that increasing Weber number increases spreading, promoting a thinner lamella, which provides less resistance to vapor bubbles bursting through.

Interestingly, the SmH surface does not exhibit the highest thermal atomization intensity. In fact, at We=20 and We=40 the amount of atomization present on the SmH surface is noticeably smaller than on the 8 µm pitch SH surface. Experiments show that lamella thickness does not change significantly between surfaces, so droplet wetting leading to greater vapor generation on the 8 µm pitch is the likely cause for enhanced atomization intensity on this surface. As Weber number increases, the difference in atomization intensity between the SmH and 8 µm pitch surfaces decreases considerably, until (at We=200) maximum atomization is virtually the same on both surfaces. Although the amount of initial wetting present on a surface increases at elevated Weber number, Pittoni [38] showed that the rate of droplet dewetting also increases with Weber number, which would reduce the impact of the additional heating which occurs due to wetting.

Both the 12 μm and 16 μm pitch SH surfaces always exhibit much less atomization than the SmH and 8 μm pitch surfaces. We

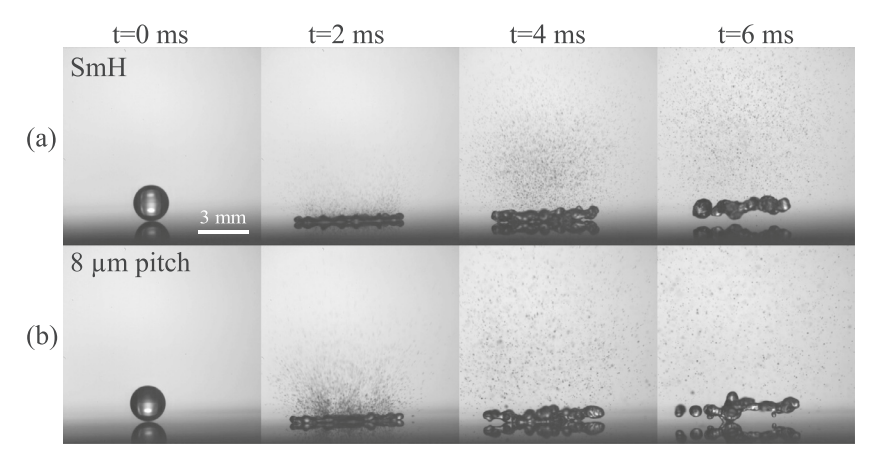


Fig. 5. Time progression of a droplet impinging the (a) SmH surface and (b) 8 μ m pitch SH surface at We = 85 and $T_s = 240$ °C.

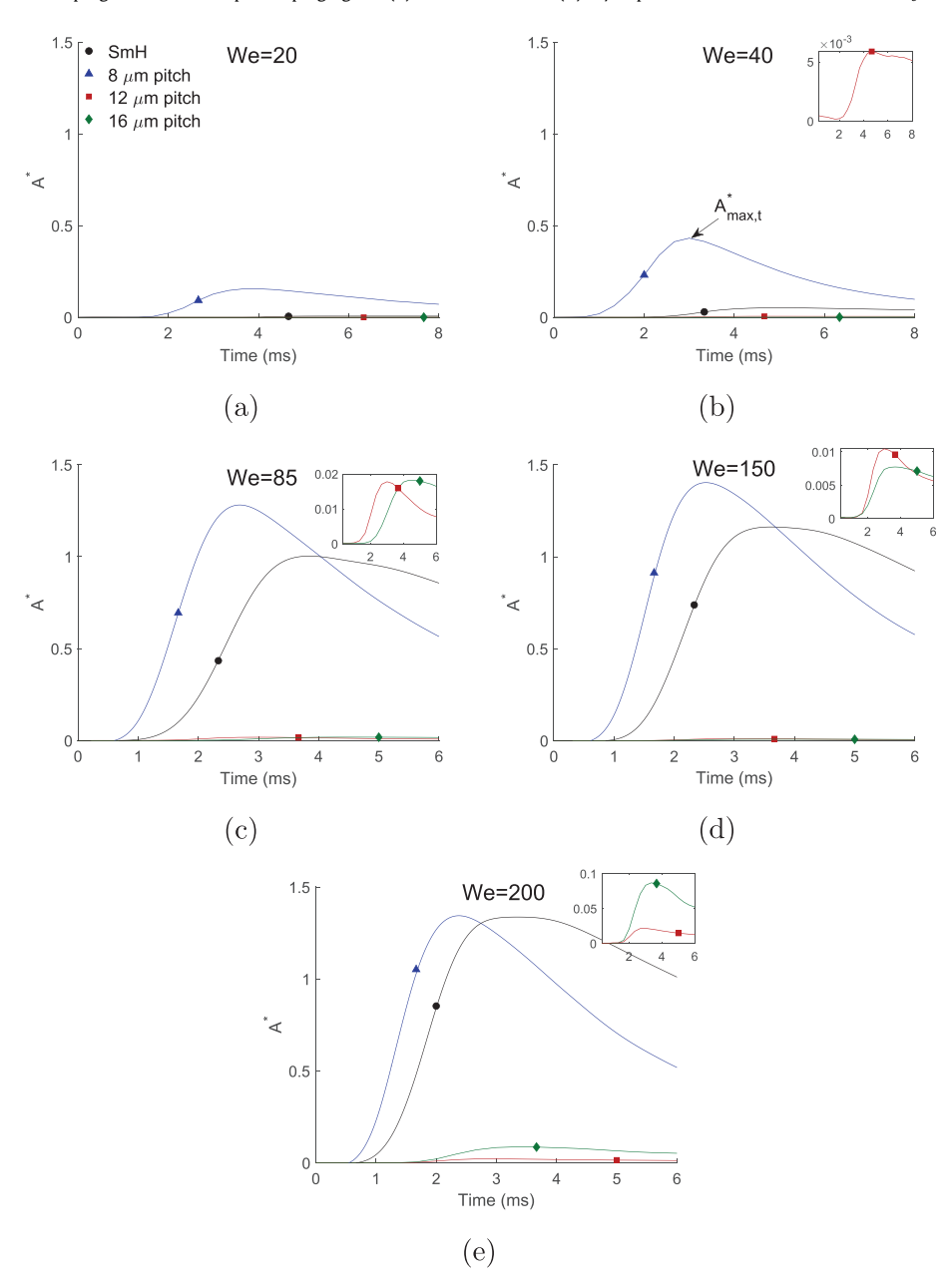


Fig. 6. Normalized atomization intensity, A^* , plotted as a function of time for each surface at (a) We = 20 (b) We = 40 (c) We = 85 (d) We = 150 and (e) We = 200. Each line corresponds to the surface temperature that results in the highest atomization intensity for each surface: 220 °C for SmH, 280 °C for 8 μm pitch, and 180 °C for 12 μm and 16 μm pitch. Plot insets display A^* with a smaller scale to show trends for the 12 μm and 16 μm pitch surfaces.

hypothesize that suppression of atomization on these surfaces is attributed mainly to their larger pitch, which allows relatively easy vapor escape beneath the droplet. It should be noted that wetting would also occur on these surfaces, but vapor escape presumably dominates over wetting effects. The slightly smaller solid fractions of these surfaces may also play a minor role in the suppression of atomization through decreased heat transfer [45]. However, a scaling model to explore the influence of vapor escape will be presented in Section 4 which shows the relative significance of pitch as opposed to cavity fraction on vapor escape. Clavijo et al. [26] showed that atomization intensity decreases with increasing pitch at We = 85. However, the results presented in Fig. 6 show that atomization on the 16 µm pitch surface is not always lower than on the 12 μ m pitch surface. This is most evident at We=200. The difficult balance between droplet wetting and vapor escape likely causes this behavior, and will be discussed further below.

Regarding the slope of A^* in Fig. 6, in regimes where A^* is increasing or decreasing, the gradient of the curve increases as Weber number increases. This is the case for all surfaces tested, and implies increasing atomization generation rate (positive gradient) and particle velocity (negative gradient) with increasing Weber number. At We = 20 and We = 40, where the SmH surface exhibits small A*, both the positive and negative gradients of the curve are small, suggesting a low generation rate and slow moving particles. The gradients for the 8 µm pitch SH surface, which exhibits significantly more atomization than the other surfaces at We = 20 and We = 40, are much steeper, suggesting larger generation rates and particle velocities. The onset time of atomization also appears to be a function of Weber number and microstructure pitch. For all surfaces tested, the atomization initiation time occurs earlier as Weber number increases. This is consistent with faster droplet spreading at higher Weber numbers, resulting in greater liquid-solid contact and a thinner lamella at earlier times. For the SH surfaces, onset time increases with increasing microstructure

Fig. 7 presents $A_{\max,t}^*$ as a function of surface temperature for each Weber number considered. Data for low atomizing scenarios are shown in the figure insets. All data show that $A^{*_{max,t}}$ increases with increasing Weber number as the droplet spreading diameter increases and the lamella thins. Boiling regimes can be roughly identified in this figure by observing trends in relative atomization intensity with surface temperature. These regimes are identified for the SmH surface in Fig. 7c. The onset temperature for atomization corresponds to the beginning of nucleate boiling, between 160 °C and 180 °C for the SmH surface. As temperature increases in the nucleate boiling regime, atomization intensity increases due to increasing vapor bubble formation in the droplet lamella. Between 220 °C and 240 °C, transition boiling begins, where atomization intensity decreases with increasing surface temperature as vapor bubbles coalesce and a vapor film is forming. This continues until the LFP is reached at 300 °C, where the droplet impinges on a stable vapor film and atomization is suppressed.

We now consider atomization intensity on each of the SH surfaces. First, comparing the 8 µm pitch surface with the SmH, the onset of nucleate boiling occurs at a lower temperature, while the onset of transition boiling occurs at a higher temperature. Thus the boiling curve is effectively broadened due to the presence of the microposts: droplet wetting increases liquid-solid contact, enhancing vapor generation and allowing for atomization at a lower surface temperature, while the combination of wetting and vapor escape effectively delays the formation of a stable vapor film at higher surface temperatures, increasing the LFP. On the 8 µm pitch surface, the LFP exceeds the experimental temperature range explored here. Additionally, atomization intensity is significantly greater on this surface than on the SmH for Weber numbers less than 200, as was noted in the discussion of Fig. 6.

For the 12 μm and 16 μm pitch surfaces, each boiling regime occurs at lower temperatures compared with the other two surfaces, especially at low Weber numbers. On these surfaces, vapor escape through the microposts should be much greater than for the 8 μm pitch SH surface, as will be shown in Section 4. This will lead to the suppression of atomization. The range of temperatures for which atomization is present on these surfaces, although small, increases modestly with increasing Weber number. For these surfaces, the LFP occurs at or before 240 $^{\circ}\text{C}$ for most scenarios. Comparing all three SH surfaces, the LFP is shown to decrease with increasing microstructure pitch.

Considering each surface individually, $A^{*\max,t}$ generally increases with Weber number. This is to be expected considering the thinner lamella associated with high Weber numbers. On both the SmH and 8 µm pitch SH surfaces, the increase in $A^{*\max,t}$ between We=20 and We=85 is much larger than the increase between We=85 and We=200. This supports the findings of Pittoni [38] discussed above, that increasing Weber number increases dewetting rates, thus decreasing wetting effects at high Weber numbers. The LFP appears to increase somewhat with Weber number for all surfaces considered here, concomitant with delayed formation of a stable vapor film.

4. Scaling analysis

A scaling analysis is presented in this section that explores one of the major mechanisms behind thermal atomization intensity on SH surfaces: vapor flow through the micropost array. We hypothesize that decreasing resistance to vapor flow through the posts (thus allowing greater vapor escape beneath the droplet) reduces the propensity for vapor bubbles to travel up through the lamella and results in the suppression of atomization. It will be shown that the resistance to flow between microposts scales with surface temperature, Weber number, and the pitch of the post array. Results of the scaling are compared to the experimental data to show that resistance to vapor flow between posts is indeed a good predictor of thermal atomization intensity.

4.1. Derivation of scaling

Droplet boiling and vapor flow between microposts are complex phenomena, and some simplifying assumptions are made for the scaling analysis. Boiling is assumed to take place in the nucleate regime, where increasing vapor generation is associated with increasing heat flux (as opposed to transition and film boiling, where vapor contributes to insulation of the droplet). The droplet is also assumed to be in the Cassie-Baxter state for the duration of impingement such that wetting effects are completely neglected. During spreading, vapor is assumed to flow radially in all directions through the microstructures beneath the droplet, from the center to the edge. We consider here vapor flow along one radial line in a direction of flow parallel to the rows of posts. Fig. 8 depicts vapor flowing between posts in this direction. A unit cell of the micropost array is defined as the area between four posts, illustrated by the dashed domain shown in Fig. 8a, where w, the width of the unit cell, is set to be equal to the pitch of the post array. The no slip condition applies where vapor is in contact with solid post, and a shear-free condition exists along all other boundaries of the unit cell. Fig. 8b shows the vapor area flow rate (volumetric flow rate normalized by post height), Q, through the unit cell. Continuity applied to the cell yields the following:

$$Q_{uc} = Q_{in} + Q_{gen} \tag{1}$$

where Q_{uc} is total vapor flow rate through the unit cell, Q_{in} is vapor flow into the unit cell from previous cells, and Q_{gen} is vapor

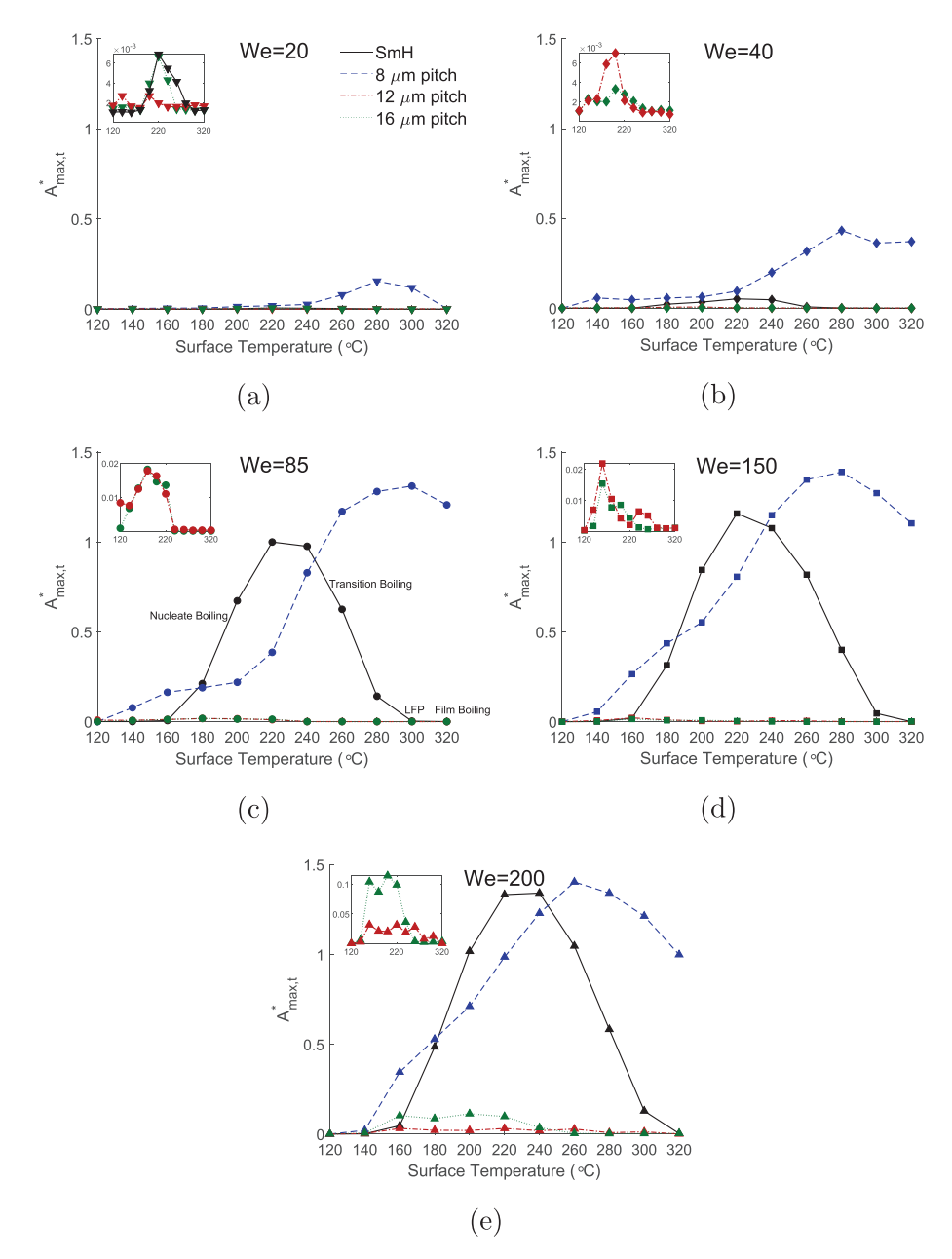


Fig. 7. Maximum normalized atomization intensity, A^* -maxe, as a function of surface temperature for all surfaces considered at (a) We = 20 (b) We = 40 (c) We = 85 (d) We = 150 and (e) We = 200. Plot insets show trends for low atomizing scenarios. In the We = 85 plot, boiling regimes and the LFP for the SmH surface are labeled.

generated due to boiling of the liquid directly above the unit cell which then enters the unit cell.

Tamayol and Bahrami [46] modeled Stokes flow through a unit cell identical to the one shown in Fig. 8a and derived the pressure drop across a unit cell, ΔP_{uc} , as a function of area flow rate:

$$\Delta P_{uc} = \frac{\mu Q_{uc}}{w^2} f(d/w) \tag{2}$$

where,

$$f(d/w) = 6 \left\{ \frac{2(d/w)}{1 - (d/w)^2} + \frac{3(d/w)^2 \left[\tan^{-1} \left(\frac{d/w}{\sqrt{1 - (d/w)^2}} \right) + \frac{\pi}{2} \right]}{\left(1 - (d/w)^2 \right)^{5/2}} \right\} + 12(1 - d/w) \left[\frac{1 + 1.274 f_s}{2} \right]$$
(3)

In Eq. (2), μ is the dynamic viscosity of the vapor. Fig. 9 depicts a line of unit cells from the center to the edge of the spreading droplet. For the purposes of this analysis, a scaling of the total pressure drop of the vapor flow beneath the spreading droplet

along this line, ΔP_{tot} , will be considered. This pressure loss corresponds directly to the total resistance to vapor flow between microposts underneath the droplet.

First, we consider the balance in Eq. (1) for the case of vapor flowing through the line of unit cells in Fig. 9, where N is the number of unit cells in the radius. For this analysis, the droplet is assumed to be at the point of maximum spread, and the number of unit cells considered can be expressed as $N = D_{\rm max}/2w$, where $D_{\rm max}$ is the diameter of maximum spread. Wildeman et al. [47] derived the maximum spreading diameter for a free-slip case as:

$$D_{\text{max}} = D_0 \sqrt{\frac{4}{1 - \cos\theta_a} \left(\frac{We}{24} + 1\right)} \tag{4}$$

where θ_a is the advancing contact angle. θ_a is nominally 160 $^\circ$ for all surfaces considered in this study. Results from our experiments show that $D_{\rm max}$ as predicted by Eq. (4) matches within 4.5% over the range of Weber numbers considered.

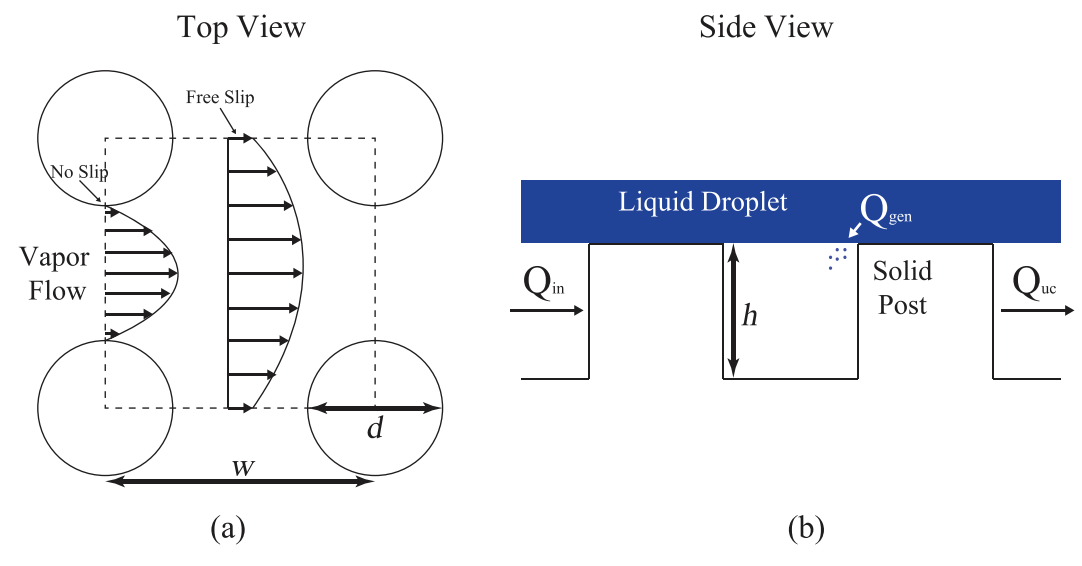


Fig. 8. Schematic of vapor flow through a unit cell of the micropost array depicting (a) a top view (unit cell is outlined by the dashed line and velocity profiles are shown) and (b) a side view showing vapor flow rate (Q) in and out of the unit cell.

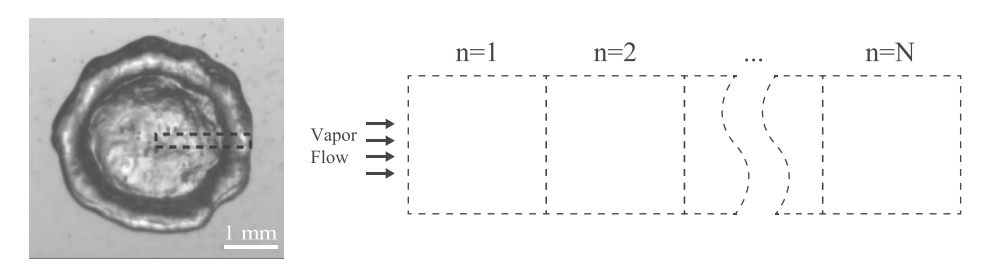


Fig. 9. Left: top-down high-speed image of a droplet impinging a SH surface 2.7 ms after impact at We = 40 and $T_s = 220$ °C. The dashed line indicates a line of unit cells from the center to the edge of the droplet. Right: schematic of vapor flow through the line of unit cells contained in the radius of the droplet, where N is the number of unit cells in the radius.

We neglect the two-dimensional nature of the flow and assume that the flow through all successive radial cells increases strictly due to the vapor generation from boiling. Vapor generation due to boiling, Q_{gen} , is assumed equal for each unit cell, and scales as:

$$Q_{\rm gen} \sim \frac{q_{\rm d}^{''} A_{\rm c}}{h_{\rm fg} \rho_{\rm vap} h} \tag{5}$$

where q_d'' is heat flux to the spreading droplet, A_c is the interfacial contact area of the unit cell (taken to be $A_c = w^2$), h_{fg} is the latent heat of vaporization for water, and ρ_{vap} is the density of water vapor. The vapor is assumed to behave as an ideal gas such that ρ_{vap} is calculated as a function of surface temperature. Heat flux to the droplet is calculated as [22,45]:

$$q_d''(t) = \frac{\sqrt{k_s \rho_s c_{p,s}} \Delta T_e}{\sqrt{\pi t}}$$
 (6)

where k_s , ρ_s , and $c_{p,s}$ are the thermal conductivity, density, and specific heat (respectively) of the SH surface, $\Delta T_e = T_s - T_{sat}$ is the excess temperature, and t is the time after droplet impact. In Eq. (6), t is taken to be the time for maximum spread, which was found experimentally to be $t_{ms} \approx 2.7$ ms irrespective of surface type or Weber number. Because the SH surfaces are composed of solid posts and air cavities, bulk surface properties are determined using the solid fraction following the approach of Guo et al. [45]: $k_s = k_{silicon}f_s + k_{air}(1 - f_s)$ and $\rho_s c_{p,s} = \rho_{silicon}c_{p,silicon}f_s + \rho_{air}c_{p,air}(1 - f_s)$. Values of the material properties for the surfaces considered here can be found in Table 2.

Table 2 Properties of materials.

Property	Water	Silicon	Air
$\rho (kg/m^3)$ $c_p (J/kgK)$ $k (W/mK)$	998	2329	1.29
	4200	700	1006
	0.6	120	0.026

Because vapor generation is the same in each unit cell, vapor flow through the *n*th unit cell can be expressed as:

$$Q_{uc,n} = nQ_{gen} \tag{7}$$

Combining Eqs. (2) and (7), the pressure drop across the nth unit cell scales as:

$$\Delta P_{uc,n} \sim \frac{n\mu Q_{gen}}{w^2} f(d/w) \tag{8}$$

The total pressure drop, ΔP_{tot} , from the center to the edge of the droplet is then calculated by summing $\Delta P_{uc,n}$ radially outward:

$$\Delta P_{tot} \sim \frac{\mu Q_{gen}}{w^2} f(d/w) \sum_{n=1}^{N} n$$
 (9)

or

$$\Delta P_{tot} \sim \frac{\mu Q_{gen}}{w^2} f(d/w) \frac{N^2 + N}{2} \tag{10}$$

4.2. Results of scaling

Scaling results are presented in this section to show how resistance to vapor flow through the micropost arrays (represented

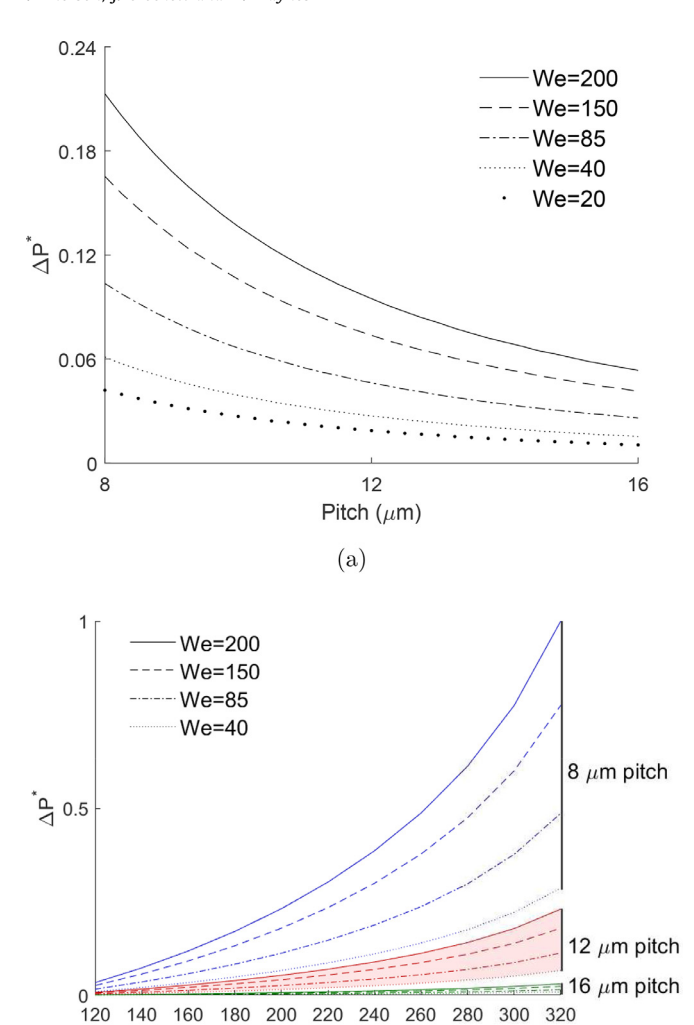


Fig. 10. (a) ΔP^* as a function of pitch for varying Weber numbers, at $T_s = 180$ °C and $f_s = 0.15$. (b) ΔP^* as a function of surface temperature on each experimental SH surface for Weber numbers of 40, 85, 150, and 200.

(b)

 $T_s(^{\circ}C)$

as pressure drop) varies with microstructure pitch, Weber number, and surface temperature. These results are compared to experimentally obtained atomization intensity to demonstrate the correlation between resistance to vapor flow and thermal atomization. Scaled pressure drop is presented as ΔP^* , the ratio of total pressure drop from the center to the edge of the droplet to the maximum value for all scenarios considered. This maximum value occurs on the 8 µm pitch surface at $T_S = 320$ °C and We = 200.

In Fig. 10a, ΔP^* is plotted as a function of surface microstructure pitch for a constant solid fraction of $f_S=0.15$. For these scenarios, a surface temperature of 180 °C was chosen, as it was observed to be in the nucleate boiling regime for all of the SH surfaces considered experimentally. It is shown from this figure that as pitch increases, ΔP^* decreases dramatically. This decrease is more significant when moving from 8 μ m to 12 μ m than when moving from 12 μ m to 16 μ m. Correspondingly, experimental data show that a much higher maximum atomization intensity is observed on the 8 μ m pitch surface than on the 12 μ m or 16 μ m pitch surfaces (see Fig. 7), supporting the hypothesis that atomization intensity decreases with decreasing resistance to vapor flow and that this is more pronounced at lower pitch. As Weber number increases, ΔP^* increases due to the increase in maximum spread

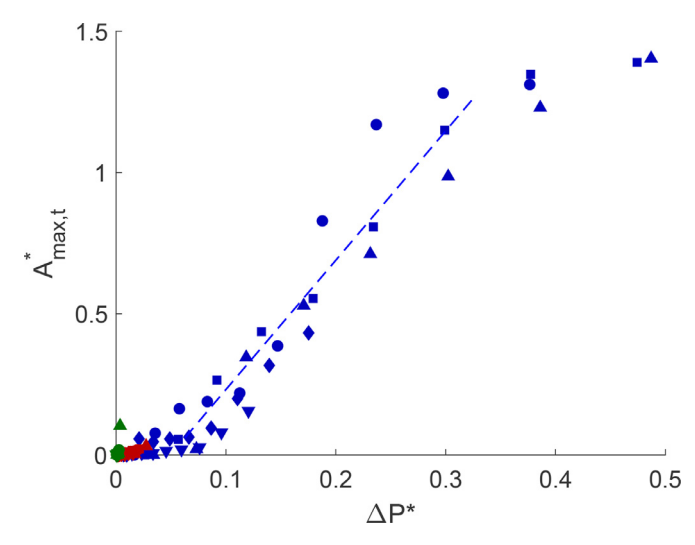


Fig. 11. A^* -max ℓ as a function of ΔP^* on all surfaces. Scenarios in the transition and film boiling regimes are left out. Blue markers represent data on the 8 μ m pitch surface, red represent the 12 μ m pitch surface, and green represent the 16 μ m pitch surface. Different Weber numbers are represented as different markers: (\P) We = 20, (\P) We = 40, (\P) We = 85, (\P) We = 150, and (\P) We = 200. The dashed line is included for convenience to show a general trend.

diameter of the droplet, resulting in greater thermal atomization, which is the case in the nucleate boiling regime for each SH surface explored, as seen in Fig. 7.

Fig. 10 b shows ΔP^* as a function of surface temperature for varying Weber number and pitch. Results are shown for each SH surface at We = 40, 85, 150, and 200. Similar to Fig. 10a, we see that ΔP^* increases with increasing Weber number. ΔP^* also increases with surface temperature due to increasing vapor generation. This is much more significant on the 8 µm pitch surface, and supports the experimental data in Fig. 7, where atomization intensity varies more with surface temperature on the 8 µm pitch surface than on the 12 µm and 16 µm pitch surfaces. We also note that ΔP^* from the scaling is nearly an order of magnitude greater on the 8 µm pitch surface than on the other SH surfaces, which supports the significantly greater atomization observed on this surface experimentally. Note that while Fig. 10b displays the entire range of experimental surface temperatures considered, the scaling breaks down as transition boiling is reached for each surface. This threshold varies with Weber number, but is nominally 280 °C on the 8 µm pitch surface, and between 180 °C and 220 °C for the 12 μm and 16 μm pitch surfaces.

Experimentally obtained atomization intensity, $A^{*_{max,t}}$, is shown in Fig. 11 as a function of ΔP^* . The dashed line is included for convenience to show a general trend. Note that scenarios that were determined to be in the transition or film boiling regimes were neglected in this plot, where these regimes were taken to be all temperatures above the maximum atomizing temperature. For each SH surface considered, $A^{*\max,t}$ is shown to be a strong function of ΔP^* , indicating that resistance to vapor flow through microstructures is indeed a good predictor of thermal atomization intensity. Given the complex nature of the impingement, boiling, and atomization processes, it is remarkable that atomization intensity shows such a strong correlation with this single parameter. Above $\Delta P^* \approx 0.3$, atomization intensity for the 8 µm pitch surface begins to flatten. This flattening suggests a point where vapor flow is completely restricted, and the maximum atomization for the surface has been achieved.

5. Conclusions

Thermal atomization intensity present during droplet impingement scenarios on superheated SmH and post-patterned SH surfaces was experimentally investigated for a range of microstructure pitches and Weber numbers. Atomization intensity in a given impingement scenario is closely correlated to the boiling regime present. Atomization increases in the nucleate boiling regime and decreases during transition boiling until the LFP is reached, whereupon film boiling dominates and atomization is suppressed.

The rate of atomization generation, atomized particle velocity, and atomization initiation time were also investigated. Atomization generation rate and particle velocity both increase with Weber number for all the surfaces studied here, with the 8 µm pitch surface always exhibiting the highest values of each. The initiation time increases with decreasing Weber number and increasing SH microstructure pitch. The LFP was found to increase with increasing Weber number and decreasing microstructure pitch.

Atomization on the SmH surface increases with Weber number due to decreasing lamella thickness. Each of the SH surfaces follows the same trend, but the microstructure configuration on these surfaces significantly alters the amount of atomization generation compared with the SmH by enabling both droplet wetting and lateral vapor escape through the micropost arrays. The 8 µm pitch surface always exhibits the greatest atomization intensity, presumably due to its low pitch, which allows intermittent wetting at high temperatures but restricts a large portion of vapor escape. However, at high Weber number, the 8 µm pitch and SmH surfaces exhibit almost identical atomization intensity, supporting findings by Pittoni [38] that wetting effects play less of a role at high Weber numbers. It was also found that on the SmH and 8 µm pitch surfaces, a maximum atomization intensity exists, beyond which increasing Weber number no longer affects the amount of atomization observed.

Both the 12 μ m and 16 μ m pitch surfaces exhibit very low atomization intensity compared with the SmH and the 8 μ m pitch as the increased pitch significantly enhances the ability for to vapor escape.

A scaling model was developed to explore the resistance to vapor flow through the SH micropost array. The scaling indicates that resistance to vapor flow, and consequently atomization intensity, increases dramatically with decreasing pitch, consistent with experimental data. Measured atomization intensity was shown to be a strong function of ΔP^* , indicating that Weber number and surface temperature both play a significant role in resistance to vapor flow, and that ΔP^* may be used to predict thermal atomization generation during nucleate boiling.

Declaration of competing interest

The authors declare that they have no known competing financial interests or personal relationships that could have appeared to influence the work reported in this paper.

CRediT authorship contribution statement

Preston Emerson: Writing - original draft, Formal analysis, Project administration. **Julie Crockett:** Funding acquisition, Conceptualization, Writing - original draft, Formal analysis, Writing - review & editing, Project administration. **Daniel Maynes:** Funding acquisition, Conceptualization, Formal analysis, Writing - review & editing, Project administration.

Acknowledgments

This material is based upon work supported by the National Science Foundation under Grant No. CBET-1707123. Additionally, this work would not have been possible without the efforts of Austin Fieldsted, who spent considerable time building the experimental setup, doing experiments, and processing data.

References

- [1] A. Yarin, Drop impact dynamics: splashing, spreading, receding, bouncing, Annu. Rev. Fluid Mech. 38 (1) (2006) 159–192, doi:10.1146/annurev.fluid.38. 050304 092144
- [2] C. Josserand, S. Thoroddsen, Drop impact on a solid surface, Annu. Rev. Fluid Mech. 48 (1) (2016) 365–391, doi:10.1146/annurev-fluid-122414-034401.
- [3] X. Deng, F. Schellenberger, P. Papadopoulos, D. Vollmer, H.-J. Butt, Liquid drops impacting superamphiphobic coatings, Langmuir 29 (25) (2013) 7847–7856, doi:10.1021/la401120j. PMID: 23697383
- [4] J. Su, I. Legchenkova, C. Liu, C. Lu, G. Ma, E. Bormashenko, Y. Liu, Faceted and circular droplet spreading on hierarchical superhydrophobic surfaces, Langmuir 36 (2) (2020) 534–539, doi:10.1021/acs.langmuir.9b03347. PMID: 31880946
- [5] L. Courbin, E. Denieul, E. Dressaire, M. Roper, A. Ajdari, H.A. Stone, Imbibition by polygonal spreading on microdecorated surfaces, Nat. Mater. 6 (9) (2007) 661–664, doi:10.1038/nmat1978.
- [6] R. Hays, D. Maynes, J. Crockett, Thermal transport to droplets on heated superhydrophobic substrates, Int. J. Heat Mass Transf. 98 (2016) 70–80, doi:10.1016/ j.ijheatmasstransfer.2016.03.011.
- [7] M. Gibbons, P. Di Marco, A. Robinson, Heat flux distribution beneath evaporating hydrophilic and superhydrophobic droplets, Int. J. Heat Mass Transf. 148 (2020) 119093, doi:10.1016/j.ijheatmasstransfer.2019.119093.
- [8] M. Gibbons, P. Di Marco, A. Robinson, Local heat transfer to an evaporating superhydrophobic droplet, Int. J. Heat Mass Transf. 121 (2018) 641–652, doi:10. 1016/j.ijheatmasstransfer.2018.01.007.
- [9] S. Misyura, Heat transfer and convection of evaporating sessile droplets in transition from superhydrophilic to superhydrophobic structured wall: optimization of functional properties, Int. Commun. Heat MassTransf. 112 (2020) 104474, doi:10.1016/j.icheatmasstransfer.2019.104474.
- [10] P. Zhu, R. Chen, L. Wang, Topography-directed hot-water super-repellent surfaces, Adv. Sci. 6 (18) (2019) 1900798, doi:10.1002/advs.201900798.
- [11] D.G. Kang, G.M. Nam, W.K. In, C.Y. Lee, Evaporation of sessile water droplet on heated surface with needle-shaped nanostructures by pre-boiling oxidation process, Exp. Therm. Fluid Sci. 101 (2019) 193–200, doi:10.1016/j. expthermflusci.2018.10.016.
- [12] M. Wei, Y. Song, Y. Zhu, D.J. Preston, C.S. Tan, E.N. Wang, Heat transfer suppression by suspended droplets on microstructured surfaces, Appl. Phys. Lett. 116 (23) (2020) 233703, doi:10.1063/5.0010510.
- [13] A. Al-Sharafi, B.S. Yilbas, H. Ali, Droplet Heat Transfer on Micropost Arrays With Hydrophobic and Hydrophilic Characteristics, Journal of Heat Transfer 140 (7) (2018), doi:10.1115/1.4039013. 072402
- [14] Z. Yan, Y. Li, A comprehensive study of dynamic and heat transfer characteristics of droplet impact on micro-scale rectangular grooved surface, Energies 11 (2018) 1390.
- [15] E. Teodori, A.S. Moita, M. Moura, P. Pontes, A. Moreira, Y. Bai, X. Li, Y. Liu, Application of bioinspired superhydrophobic surfaces in two-phase heat transfer experiments, J. Bionic Eng. 14 (3) (2017) 506–519, doi:10.1016/S1672-6529(16) 60417-1
- [16] J.H. Moon, M. Cho, S.H. Lee, Dynamic wetting and heat transfer characteristics of a liquid droplet impinging on heated textured surfaces, Int. J. Heat Mass Transf. 97 (2016) 308–317, doi:10.1016/j.ijheatmasstransfer.2016.02.041.
- [17] M. Searle, P. Emerson, J. Crockett, D. Maynes, Influence of microstructure geometry on pool boiling at superhydrophobic surfaces, Int. J. Heat Mass Transf. 127 (2018) 772–783, doi:10.1016/j.ijheatmasstransfer.2018.07.044.
- [18] P. Pontes, R. Cautela, E. Teodori, A.S. Moita, A. Georgoulas, A.L.N.M. Moeira, Bubble dynamics and heat transfer on biphilic surfaces: experiments and numerical simulation, J. Bionic Eng. 17 (2020) 809–821, doi:10.1007/ s42235-020-0064-x.
- [19] J.D. Bernardin, C.J. Stebbins, I. Mudawar, Mapping of impact and heat transfer regimes of water drops impinging on a polished surface, Int. J. Heat Mass Transf. 40 (2) (1997) 247–267, doi:10.1016/0017-9310(96)00119-6.
- [20] V. Bertola, An experimental study of bouncing Leidenfrost drops: comparison between newtonian and viscoelastic liquids, Int. J. Heat Mass Transf. 52 (7–8) (2009) 1786–1793, doi:10.1016/ji.ijheatmasstransfer.2008.09.028.
- [21] V. Bertola, An impact regime map for water drops impacting on heated surfaces, Int. J. Heat Mass Transf. 85 (2015) 430–437, doi:10.1016/j. ijheatmasstransfer.2015.01.084.
- [22] J. Breitenbach, I.V. Roisman, C. Tropea, Drop collision with a hot, dry solid substrate: heat transfer during nucleate boiling, Phys. Rev. Fluids 2 (7) (2017), doi:10.1103/physreyfluids.2.074301.
- [23] I.V. Roisman, J. Breitenbach, C. Tropea, Thermal atomisation of a liquid drop after impact onto a hot substrate, J. Fluid Mech. 842 (2018) 87–101, doi:10. 1017/jfm.2018.123.
- [24] C.E. Clavijo, J. Crockett, D. Maynes, Hydrodynamics of droplet impingement on hot surfaces of varying wettability, Int. J. Heat Mass Transf. 108 (2017) 1714– 1726, doi:10.1016/j.ijheatmasstransfer.2016.12.076.

- [25] G. Liang, I. Mudawar, Review of drop impact on heated walls, Int. J. Heat Mass Transf. 106 (2017) 103–126, doi:10.1016/j.ijheatmasstransfer.2016.10.031.
- [26] C. Clavijo, K. Stevens, J. Crockett, D. Maynes, Thermally induced atomization during droplet impingement on superheated hydrophobic and superhydrophobic surfaces, Int. J. Heat Mass Transf. 126 (2018) 1357–1366, doi:10.1016/j. ijheatmasstransfer.2018.05.068.
- [27] D. Antonov, N. Shlegel, P. Strizhak, D. Tarlet, J. Bellettre, Energy analysis of secondary droplet atomization schemes, Int. Commun. Heat MassTransf. 117 (2020) 104666, doi:10.1016/j.icheatmasstransfer.2020.104666.
- [28] H. Liu, B. Chen, L. Feng, Y. Wang, W. Yi, M. Yao, Study on fuel distribution of wall-impinging diesel spray under different wall temperatures by laser-induced exciplex fluorescence (lief), Energies 11 (2018) 1249.
- [29] B. Chen, L. Feng, Y. Wang, T. Ma, H. Liu, C. Geng, M. Yao, Spray and flame characteristics of wall-impinging diesel fuel spray at different wall temperatures and ambient pressures in a constant volume combustion vessel, Fuel 235 (2019) 416–425, doi:10.1016/j.fuel.2018.07.154.
- [30] X. Yu, R. Hu, X. Zhang, B. Xie, X. Luo, Explosive bouncing on heated silicon surfaces under low ambient pressure, Soft Matter (2019), doi:10.1039/ C9SM00455F.
- [31] G. Liang, S. Shen, Y. Guo, J. Zhang, Boiling from liquid drops impact on a heated wall, Int. J. Heat Mass Transf. 100 (2016) 48–57, doi:10.1016/j. ijheatmasstransfer.2016.04.061.
- [32] Deendarlianto, Y. Takata, A. Widyatama, A.I. Majid, A. Wiranata, A. Widyaparaga, M. Kohno, S. Hidaka, Indarto, The interfacial dynamics of the micrometric droplet diameters during the impacting onto inclined hot surfaces, Int. J. Heat Mass Transf. 126 (2018) 39–51, doi:10.1016/j.ijheatmasstransfer.2018.05.023
- [33] Q. Ma, X. Wu, T. Li, F. Chu, Droplet boiling on heated surfaces with various wettabilities, Appl. Therm. Eng. 167 (2020) 114703, doi:10.1016/j. applthermaleng.2019.114703.
- [34] M. Auliano, M. Fernandino, P. Zhang, C.A. Dorao, Water droplet impacting on overheated random Si nanowires, Int. J. Heat Mass Transf. 124 (2018) 307–318, doi:10.1016/j.ijheatmasstransfer.2018.03.042.

- [35] S.H. Kim, Y. Jiang, H. Kim, Droplet impact and LFP on wettability and nanos-tructured surface, Exp. Therm. Fluid Sci. 99 (2018) 85–93, doi:10.1016/j.expthermflusci.2018.07.029.
- [36] C. Ishino, M. Reyssat, E. Reyssat, K. Okumura, D. Quéré, Wicking within forests of micropillars, Europhys. Lett. (EPL) 79 (5) (2007) 56005, doi:10.1209/ 0295-5075/79/56005.
- [37] T. Deng, K.K. Varanasi, M. Hsu, N. Bhate, C. Keimel, J. Stein, M. Blohm, Non-wetting of impinging droplets on textured surfaces, Appl. Phys. Lett. 94 (13) (2009) 133109, doi:10.1063/1.3110054.
- [38] P.G. Pittoni, Y.-C. Lin, S.-Y. Lin, The impalement of water drops impinging onto hydrophobic/superhydrophobic graphite surfaces: the role of dynamic pressure, hammer pressure and liquid penetration time, Appl. Surf. Sci. 301 (2014) 515–524, doi:10.1016/j.apsusc.2014.02.115.
- [39] C.E. Clavijo, J. Crockett, D. Maynes, Wenzel to Cassie transition during droplet impingement on a superhydrophobic surface, Phys. Rev. Fluids 1 (7) (2016), doi:10.1103/physrevfluids.1.073902.
- [40] J. Field, ELSI conference: invited lecture, Wear 233-235 (1999) 1-12, doi:10. 1016/s0043-1648(99)00189-1.
- [41] T. Tran, H.J.J. Staat, A. Prosperetti, C. Sun, D. Lohse, Drop impact on superheated surfaces, Phys. Rev. Lett. 108 (3) (2012), doi:10.1103/physrevlett.108.036101.
- [42] A. Rozhkov, B. Prunet-Foch, M. Vignes-Adler, Impact of water drops on small targets, Phys. Fluids 14 (10) (2002) 3485–3501, doi:10.1063/1.1502663.
- [43] P.-G. de Gennes, F. Brochard-Wyart, D. Quere, Capillarity and Wetting Phenomena: Drops, Bubbles, Pearls, Waves, Springer, Berlin, 2004.
- [44] E.Y. Bormashenko, Physics of Wetting, De Gruyter, Berlin, Boston, 11 Sep. 2017, doi:10.1515/9783110444810.
- [45] C. Guo, D. Maynes, J. Crockett, D. Zhao, Heat transfer to bouncing droplets on superhydrophobic surfaces, Int. J. Heat Mass Transf. 137 (2019) 857–867, doi:10.1016/j.ijheatmasstransfer.2019.03.103.
- [46] A. Tamayol, M. Bahrami, Analytical determination of viscous permeability of fibrous porous media, Int. J. Heat Mass Transf. 52 (9–10) (2009) 2407–2414, doi:10.1016/j.ijheatmasstransfer.2008.09.032.
- [47] S. Wildeman, C.W. Visser, C. Sun, D. Lohse, On the spreading of impacting drops, J. Fluid Mech. 805 (2016) 636–655, doi:10.1017/jfm.2016.584.